Taylor & Francis
Taylor & Francis Group

Multiscale creep characterization and modeling of a zirconia-rich fused-cast refractory

Kamel Madi[a]*, Sylvain Gailliègue[a], Michel Boussuge[a], Samuel Forest[a], Michel Gaubil[b], Elodie Boller[c] and Jean-Yves Buffière[d]

[a]*Mines-ParisTech, CNRS-UMR 7633-Centre des Matériaux, BP 87, 91003 Evry, France;* [b]*Centre de Recherches et d'Etudes Européen (CREE)/Saint-Gobain, Cavaillon, France;* [c]*European Synchrotron Radiation Facility, BP220, 38043 Grenoble Cedex, France;* [d]*INSA-Lyon, MATEIS, CNRS UMR 5510, 69621 Villeurbanne, France*

This work aims at investigating the mechanical behaviour of a zirconia-rich fused-cast refractory at high temperature (1400 °C). The geometry of the zirconia phase was analysed on samples having contents of amorphous phase ranging from 12 to 24% in volume, from 3D images obtained using the X-ray computed micro-tomography technique. The sharp intrication of the dendrites creates a continous zirconia skeleton which was characterized experimentally. Results at high temperature show that deformation is controlled by zirconia, whereas the amorphous phase does not play any structural role. Finite-element simulations have been carried out to predict the creep behaviour of the aggregate. The creep law of the zirconia skeleton was identified by an inverse method from a creep test at 1400 °C and from the 3D real morphology of the dendritic zirconia structure. Simulation results confirm that the rheology of the aggregate is controlled by the zirconia skeleton and a good agreement was observed between numerical creep tests and experiments.

Keywords: creep; zirconia; glassy phase; tomography; dendritic structure; finite element

1. Introduction

Demand for new high-quality glasses requires a better knowledge of the design and optimization of glass furnaces. Fused-cast refractories are good candidates for this challenge. In particular, the family of zirconia-rich fused-cast refractories is well known for their outstanding creep and corrosion resistance at high temperature [1]. These materials are constituted mainly of zirconia (88% vol.), i.e. the hard phase, surrounded by a thin layer of amorphous phase (12% vol.), i.e. the weak phase. Their manufacturing process is similar to the metallurgical foundry, which consists in melting raw materials at very high temperature (2500 °C), casting the liquid into molds and then cooling down. The cooling stage is a critical step in the fabrication process that can strongly influence the quality of the final product. During the manufacturing process, the materials undergo several constraints [1,2]:

*Corresponding author. Email: kamel.madi@port.ac.uk
Kamel Madi is now at Mechanical Behaviour of Materials, Department of Mechanical and Design Engineering, University of Portsmouth, UK.

high-thermal gradients, creep at high temperature and zirconia phase transformation (around 1000 °C during the cooling). These constraints can affect the mechanical behaviour leading to damage, microcracking at temperatures lower than the glass transition temperature of the amorphous phase, and extension of the damage during several days at room temperature (stress corrosion).

Understanding the complex thermomechanical processes affecting refractories, in service and during the manufacturing process, is of paramount importance to facilitate their fabrication, increase the lifetime of the glass furnaces and improve the development of new refractory products. This was the goal fixed by the research programme PROMETHEREF [3], undertaken by a federation of industrial companies and university research centres. Several research works were carried out to characterize and predict the mechanical behaviour of different refractrories using multiple complementary techniques [4–11] at different scales; namely, scale of the refractory block, sample scale and scale of the microstructure.

The mechanical behaviour of the fused-cast refractories at high temperature is difficult to predict due to their complex microstructure and huge contrast between the mechanical properties of their constituents. Analytical models, like the Reuss and Taylor bounds, are too far apart to give a useful estimate of the effective properties. A more realistic description can be obtained by using the viscoplastic self-consistent approach [12–14] or the differential approach [15]. These methods have been shown to provide robust solutions in rocks, porous media and metallic materials, but correspond to a very specific component morphology.

A different approach consists in using finite-element modelling, which introduces explicitely the morphology of the heterogeneous materials being considered (including phase distribution). This technique has proven to be a very powerful tool to understand and predict the mechanical behaviour of cellular materials [16–20]. This method proved also to be very efficient in predicting, with a reasonably good agreement with experiments, the mechanical properties of 3D metallic aggregates with realistic morphologies [21–26]. Recently, this approach has been used to predict the elastic behaviour of zirconia-rich fused-cast refractories [11].

This paper is a follow up to the work proposed in [11]. In the latter, the authors investigated the 3D connectivity of the phases using the concept of geometrical percolation. They showed that both phases are spatially interconnected and that the 3D connectivity of the zirconia phase is a possible explanation for the high creep and corrosion resistance observed at high temperature. A 3D finite-element model, which takes into account the 3D real morphology of the microstructure, was developed and elastic computations were performed for different contents of amorphous phase. Due to the high percolation of the zirconia phase, a high stiffness was predicted, even for large amorphous phase content.

The development of the microstructure during solification depends on various parameters such as the solidification rate, temperature gradients, composition, growth kinetics of the phases and crystallographic constraints [27,28]. Under solidification conditions encountered in casting of zirconia-rich fused-cast refractories, the zirconia crystallization leads to a saturated dendritic microstructure. Owing to the sharp imbrication of the dendrites [29–31], the zirconia phase can be considered like an interlocked continuous skeleton. In addition, the nature and amount of additives change the topology of the microstructure during solidification, which in turn controls the macroscopic mechanical properties. Understanding the relationship between these three variables is crucial to optimise the products. The present work aims at investigating the link between the amorphous phase content, the zirconia skeleton morphology and the creep behaviour at high temperature.

Samples with different contents of amorphous phase (18% vol. and 24% vol.) were machined from small refractory blocks fabricated by Saint-Gobain and scanned using the X-ray microtomography technique. Increasing the amount of amorphous phase leads to an increase of the interdendritic spaces and a better view of the dendrite arms. The 3D images were then analysed using different concepts of mathematical morphology to investigate the geometry of the zirconia skeleton. Secondly, creep tests were performed at high temperature on a porous zirconia skeleton, obtained after chemically removing the amorphous phase, and compared to the as-received material.

The creep behaviour of the material was also simulated at the scale of the microstructural constituents, taking advantage of the recent progress of 3D finite-element modelling. A creep law of the zirconia skeleton was identified at 1400 °C by an inverse method, using its 3D real morphology. The contribution of the amorphous phase to the overall response was investigated and the results were compared to the experiments.

2. Materials and experimental procedure

2.1. *Materials*

The material of the study is a dense zirconia-rich fused-cast refractory, mainly constituted of zirconia (88% vol.) permeated by a darker thin-layer of amorphous phase (see Figure 1(a)). This material is called ZS12 in the following. The chemical composition of the amorphous phase is reported in Table 1. To study the impact of the amorphous phase content on the mechanical behaviour of the material, two extra materials were fabricated by the CREE (Centre de Recherche et d'Etudes Européen) of Saint-Gobain in Cavaillon (France). They were fabricated using the same process but their dimensions were much smaller than the industrial ones. The samples were prepared according to a protocol defined in the PROMETHEREF research programme [3]. The samples were extracted from the core of refractory blocks by taking precautions to obtain representative isotropic specimens and to avoid tempering effects. They are called ZS18 for the material containing 18% of amorphous phase and ZS24 for the one containing 24% of amorphous phase. Increasing the amount of amorphous phase better reveals the layer of amorphous phase, as illustrated in 2D microstructural observations (see Figure 1(b) and (c)). From 2D observations, the microstructure seems to be constituted of individual zirconia entities surrounded by the amorphous phase, similar to sintered materials. The size of these entities was characterized using a granulometry algorithm, which consists in performing series of morphological openings with structuring elements of increasing size [32,33]. Average diameters $d^{ZS12} = 200 \pm 73\,\mu$m, $d^{ZS18} = 117 \pm 38\,\mu$m and $d^{ZS24} = 79 \pm 22\,\mu$m were found, respectively, for ZS12, ZS18 and ZS24. The size decreases with increasing volume fraction of amorphous phase. This observation will be discussed in Section 4.1, along with a detailed analysis of the 3D microstructure (Sections 4.2 and 4.3).

Table 1. Chemical composition of the amorphous phase contained in the ZS12 material, given in percentage according to weight [4].

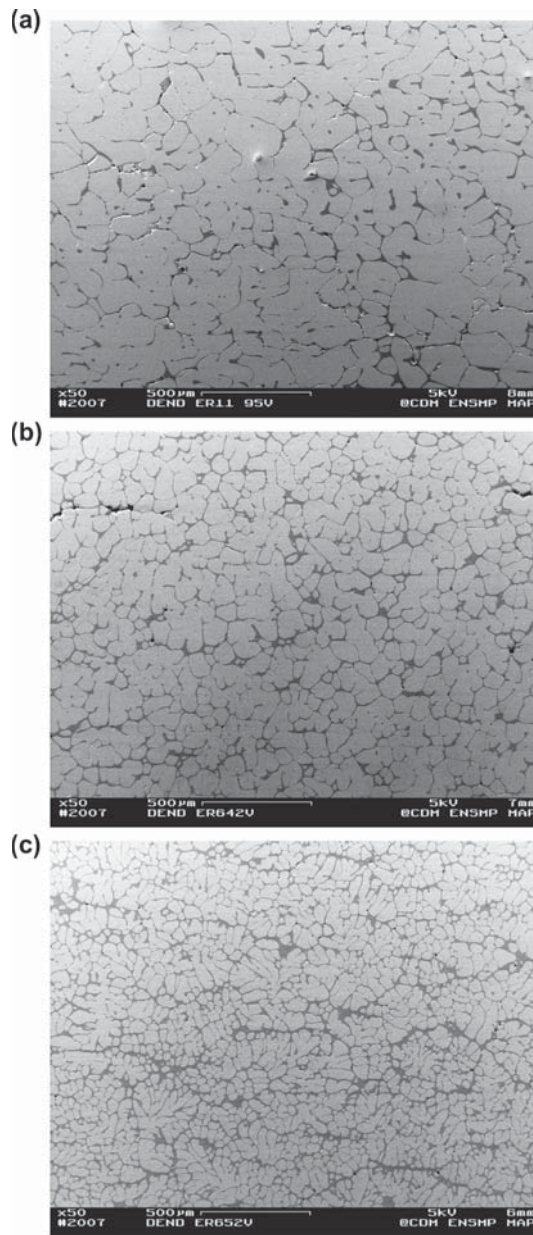| Chemical element	ZrO_2	SiO_2	Al_2O_3	Na_2O	TiO_2	Fe_2O_3	Al_2O_3/Na_2O
Weight percent	1	73	19	5.3	0.5	0.35	3.8

Figure 1. SEM images of the materials (secondary electrons imaging): (a) ZS12 material (12% of amorphous phase), (b) ZS18 material (18% of amorphous phase), (c) ZS24 material (24% of amorphous phase). The microstructure seems to be constituted of zirconia entities, surrounded by the amorphous phase, with an average diameter $d^{ZS12} = 200 \pm 73\mu$m for ZS12, $d^{ZS18} = 117 \pm 38\mu$m for ZS18 and $d^{ZS24} = 79 \pm 22\mu$m for ZS24.

2.2. *3D representation of the morphology*

To get a 3D representation of the material, high energy X-ray tomography at the European Synchrotron Radiation Facility (ESRF, Grenoble, France) was used. This technique consists in recording several radiographs of a sample at different angular positions. A 3D map of the X-ray attenuation coefficient within the material is then built using adequate algorithm and software [34]. This technique can reveal all the microstructural features (inclusions, cracks, pores, constituting phases, etc.) that induce a change in attenuation along the path of the X-ray beam. A high contrast exists between the high X-ray attenuation of zirconia compared to that of the amorphous phase. Figure 2 illustrates 3D images of the microstructure of the three materials obtained with a high resolution (size of the detector pixel: 0.7 μm). The ID19 beamline was used, with an X-ray energy of 40 keV. Before quantification, the
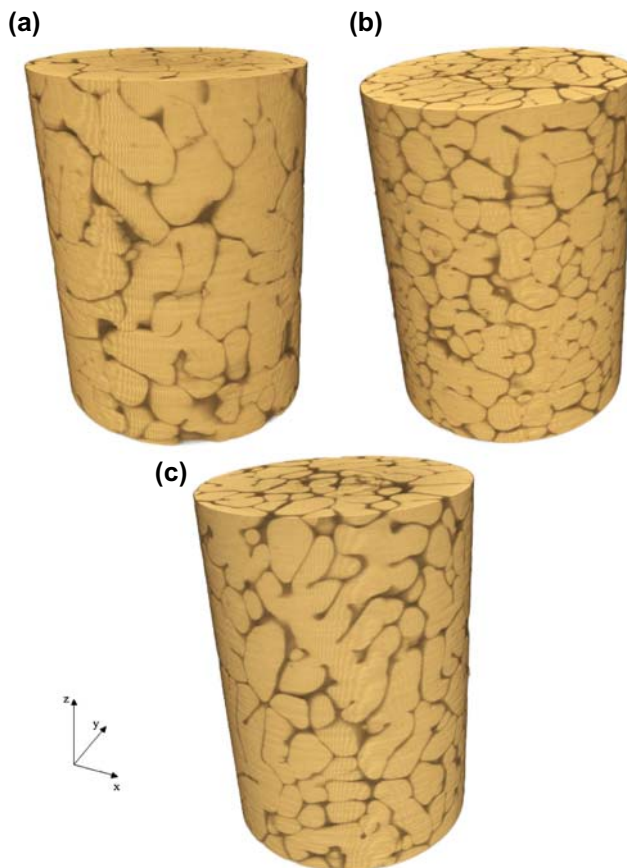

Figure 2. (colour online) 3D representations of zirconia-rich fused-cast refractories cylinders, obtained using X-ray micro-computed tomography at the synchrotron of Grenoble (ESRF): (a) ZS12 ($f_v^{ZS12} = 12\%$), (b) ZS18 ($f_v^{ZS18} = 18\%$), (c) ZS24 ($f_v^{ZS24} = 24\%$). The zirconia and the amorphous phase are yellow and dark, respectively. The cylinders have a diameter of 500 μm (714 pixels) and a height of 1433 μm (2048 pixels).

images were cleaned and binarised using the procedure described in [11]. A robust filter was used to eliminate partial rings artefacts (marked circular patterns attributed to a non-linear behaviour of some pixels of the detector during the imaging) without pertubating the rest of the image [35,36]. After this cleaning step, the method used to segment our images consisted in choosing a threshold, using an histogram of grey levels as a guide. In our case, the choice of the threshold was quite easy due to the high contrast between the phases.

2.3. *3D characterization of the morphology*

In this section, basic morphological tools available to quantitatively characterize the geometry of the phases are introduced.

2.3.1. *Covariance*

The covariance $C(h)$ [32,33,37,38] is the probability for two points, separated by a vector h, to belong to the same stationary random set A. We have:

$$C(h) = P(x \in A, x + h \in A) = P(x \in A \cap A_{-h}) \tag{1}$$

which is estimated from the measurement of the volume fraction V_v (deduced from the number of voxels in one set) of the intersection of the set A and the translate of A by the vector h:

$$C(h) = V_v(A \cap A_{-h}) \tag{2}$$

This measurement is sensitive to the heterogeneity of the spatial distribution and to the anisotropy, provided that the sample is representative of the investigated microstructure. When $h = 0$, the covariance $C(h)$ is equal to $V_v^A = p$, the volume fraction of the set A (i.e. the amorphous phase or the zirconia phase). If the events $(x \in A)$ and $(x + h \in A)$ become independent as the magnitude of h becomes large, then $C(h)$ converges to p^2 as h increases. The value of h for which this asymptote is reached is the correlation length (or range) of the considered phase. Only the zirconia phase is considered in the present study. This value is called L_z. It is characteristic of the size and arrangement of the zirconia phase and can be interpreted as the scale over which the volume fraction of zirconia fluctuates.

2.3.2. *3D connectivity of the phases*

The 3D connectivity of the phases has been investigated using the concept of geometrical percolation [11,39]. Using image analysis tools and a mathematical morphology algorithm, based on the 3D geodesic reconstruction, two important concepts are defined: (i) the image of the interconnected phase, defined as the set of all points in a given phase that can be connected to two opposite sides of the image following paths entirely contained in the same phase; (ii) the percolation index, defined as the ratio between the volume fraction of the interconnected phase to the whole volume fraction in the microstructure of this phase. It is always lower than or equal to 1. It is equal to 1 if the whole phase is interconnected and equal to zero if there is no percolation of this phase (physically this means that this phase is made of isolated inclusions).

2.3.3. *Tortuosity*

The tortuosity in every point of each investigated phase is defined as the distance of shortest paths through this point, connecting two opposite faces of the 3D image, normalised by the distance between the faces. The morphological tortuosity corresponds to the ratio between the geodesic distance and the Euclidian distance, between two parallel faces of the image, according to a direction of propagation. The minimum tortuosity is then equal to 1 by definition. The geodesic distance has been processed both in the amorphous phase and in the zirconia phase. The method that we used to estimate the geodesic lengths of the paths in each phase was based on geodesic propagation. The algorithm was proposed by Decker et al. [40] and implemented by Lerallut in the Morphée code [41].
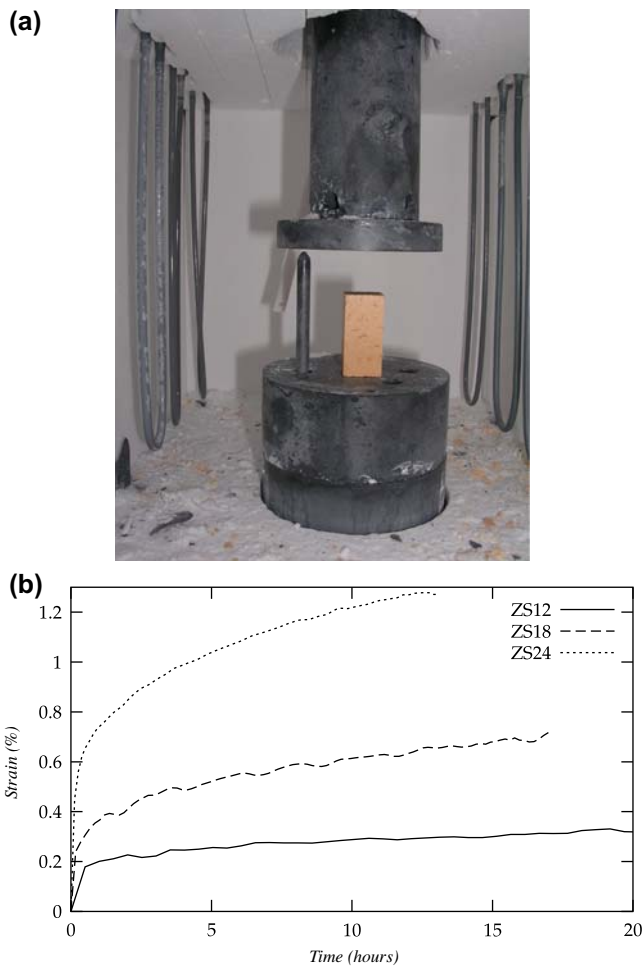

Figure 3. (colour online) (a) Inside view of the experimental compression device (SCHENCK), (b) creep deformations at T = 1400 °C obtained for the three materials under a stress of 12 MPa.

2.4. *Testing procedure*

Compressive creep tests were performed in our laboratory on each material at high temperature (1400 °C), under stresses ranging from 10 MPa to 20 MPa. The samples were parallelepipedic with dimensions of $12 \times 15 \times 30$ mm. They were tested using a Schenck compression machine, equipped with a furnace heated by molybdenum disilicide resistors [42,43]. Temperatures up to 1500 °C can be reached with this furnace. Displacement was measured below the furnace, by means of a linear variable differential transformer sensor. The measured value is the result of the relative displacements of two silicon carbide (SiC) translating rods; one in contact with the top loading SiC platen and the other in contact with the base SiC platen, which was supporting the sample (see Figure 3(a)). This differential system provides reliable measurements, with a resolution of about 1μm, independent on the dilatations of the device. Typical creep curves, obtained on each material at 1400 °C under a stress of 12 MPa applied after a temperature dwell of 2 h, are represented in Figure 3(b).
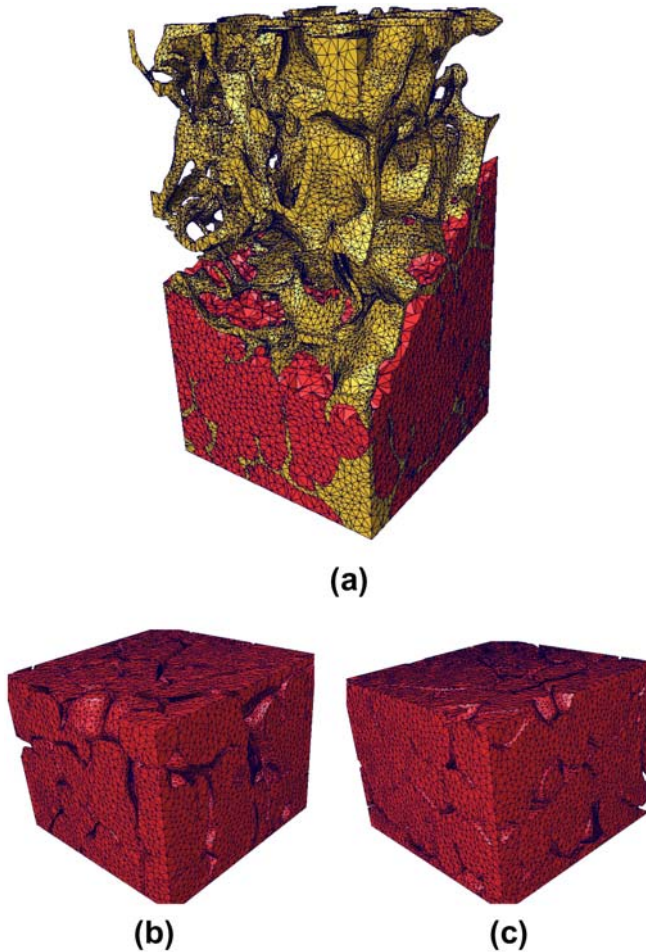

Figure 4. (colour online) (a) 3D meshing of the ZS12 material using 10-node quadratic tetrahedra (the zirconia and the amorphous phase are red and yellow respectively), (b) and (c) two representations (full specimens) of the zirconia skeleton contained in the ZS12 material. Volume dimensions are: $336 \times 310 \times 300$ μm.
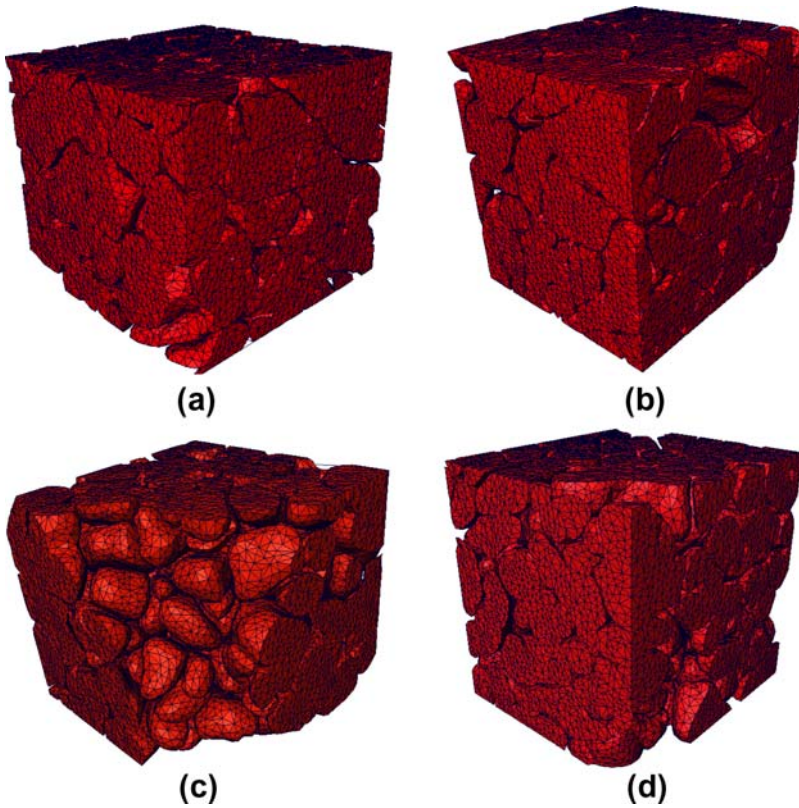
Figure 5. (colour online) 3D meshing of the zirconia skeletons contained in the ZS18 and ZS24 materials using 10-node quadratic tetrahedra: (a) ZS18 (realization 1: $fv^z = 82.76\%$), (b) ZS18 (realization 2: $fv^z = 82\%$), (c) ZS24 (realization 1: $fv^z = 75.52\%$), (d) ZS24 (realization 2: $fv^z = 78.15\%$). fv^z represents the volume fraction of zirconia. Volume dimensions are: $336 \times 310 \times 300\,\mu m$.

3. Computational method

3.1. *Finite-element meshing*

This paragraph describes the available meshing techniques based on tomographic images. The methodology used in this work, explained in [11], included three steps: (i) segmentation (in our case binarization) of the tomographic grey-level image to deconvoluate the phases, (ii) geometrical definition of the solid boundaries by triangular facets and (iii) tetrahedral meshing of the solid volume from the triangles. The second step is very important as it allows to capture the boundary between the two phases (the isosurface) and is known as triangulation. This stage was performed automatically by generating a triangulated surface model, with correct topology and optimised triangular shape, from the segmented tomographic data. This has been done using the marching cubes algorithm [19,44], implemented in the Avizo software [45]. In the last step, an unstructured tetrahedral mesh is built from the basis of the surface triangulation. Here, meshing has been performed using the advancing front method implemented in the Avizo software [46]. Figures 4 and 5 illustrate such 3D grids of the constituents of the ZS12, ZS18 and ZS24 microstructures, based on 10-node quadratic tetrahedra, obtained from the stack of segmented images illustrated in Figure 2.

3.2. *Properties of the constituents*

In this section, the high temperature mechanical properties of the constituents are detailed. The data will be introduced in the finite-element model, in order to simulate the viscoplastic behaviour of the ZS12 material at 1400 °C.

3.2.1. *Zirconia*

The elastic properties of the tetragonal zirconia at 1400 °C were deduced from the work of Yeugo-Fogaing [7]. They are reported in Table 2. Unfortunately, no experimental creep data was available in the literature for the zirconia phase contained in the fused-cast refractories. Most of the works concerned sintered and doped materials [47–55] whose microstructure is made of individual separated grains surrounded by an amorphous phase. This configuration is very different from the dendritic intricated microstructure of fused-cast refractories (see Figure 2(a)). For this reason, in this work, a new experimental procedure was developed to characterize the creep behaviour of the zirconia phase. This procedure, detailed in Sections 4.4 and 4.5, allowed the characterization of the zirconia skeleton and the identification of a creep law at 1400 °C, from a numerical model based on the 3D real morphology of the zirconia. This section will only be concerned by the creep law and the associated material coefficients.

Table 2. Mechanical data for the two phases at 1400 °C.

Phase	E (GPa)	n	K (MPa.s$^{1/n}$)	C (MPa)	D
Zirconia	186	1.73	255000	4808	41
Amorphous phase	74	1	0.002	/	/

The constitutive equations used for modelling the creep response of the zirconia phase are based on a standard elastoviscoplastic framework. The total strain is shared into elastic and plastic parts, and Hooke's law is adopted [56]:

$$\varepsilon_{ij} = \varepsilon_{ij}^e + \varepsilon_{ij}^p, \quad \sigma_{ij} = c_{ijkl}\varepsilon_{kl}^e \tag{3}$$

The selected creep law is a power law with non-linear kinematic hardening:

$$\dot{\varepsilon}_{ij}^p = \dot{p}\frac{3}{2}\frac{s_{ij} - X_{ij}}{J_2(\sigma_{ij} - X_{ij})}, \quad \dot{p} = \left(\frac{J_2(\sigma_{ij} - X_{ij})}{K}\right)^n, \tag{4}$$

$$J_2(\sigma_{ij} - X_{ij}) = \sqrt{\frac{3}{2}(s_{kl} - X_{kl})(s_{kl} - X_{kl})}, \quad \dot{X}_{ij} = \frac{2}{3}C\dot{\varepsilon}_{ij}^v - DX_{ij}\dot{p} \tag{5}$$

J_2 denotes the second invariant of the stress tensor and is also called the von Mises equivalent stress. The deviatoric part of the stress tensor is s_{ij} and p is the cumulative equivalent viscoplastic strain. n and K are the two parameters of Norton's law. X_{ij} is the kinematic hardening tensor also called back-stress tensor. The evolution of the back stress is based on a linear hardening law and a recovery term. C and D are material parameters describing the kinematic hardening [56]. Equations (4) and (5) allow both primary and secondary creep to be described. Thus, four parameters are necessary to completely define

the creep law at 1400 °C: n, K, C, D. They are reported in Table 2, together with Young's moduli. At this temperature, the yield limit is zero. These constitutive equations were implemented in the finite-element program Z-set [57]. They were integrated numerically using an implicit Newton algorithm.

3.2.2. *Amorphous phase*

The thermal expansion measurements performed at ENSCI Limoges [7] showed that the glass transition temperature of the amorphous phase, T_g, is close to 780 °C. Moreover, viscosity measurements as a function of temperature, performed at Centre de Recherche d'Aubervilliers Saint-Gobain, revealed that the viscosity of the amorphous phase decreases progressively ($log(\eta_{(Poises)}) = 13$ for $T = T_g$) with increasing temperature to reach $log(\eta_{(Poises)}) = 4$ at 1400 °C. Thus, we assumed that the amorphous phase behaves like a Newtonian fluid at 1400 °C. Rigourously, at 1400 °C, one should consider the flow of the amorphous phase in a fluid mechanics framework, which implies the resolution of a complex fluid–solid coupled problem. To simplify, the flow of the amorphous phase was approached by a Norton type power law without hardening:

$$\dot{\varepsilon}_{ij}^v = \left(\frac{J_2(\sigma_{ij})}{K} \right)^n \frac{3}{2} \frac{s_{ij}}{J_2(\sigma_{ij})} \tag{6}$$

where J_2 and s_{ij}, are respectively, the second invariant and the deviatoric part of the stress tensor, $n = 1$ and $K = 2\eta$. The flow stress K is deduced from the value of the viscosity η of the amorphous phase at 1400 °C (see Table 2). It is worth noting that the flow stress at 1400 °C is negligible, which illustrates that the amorphous phase behaves as a viscous fluid: it undergoes high deformation rates even for very low deviatoric stresses.

3.3. *Boundary conditions*

The computation cost limits the size of the volume element V that can be handled in the simulation. Such a size might be smaller than a so-called representative volume element of the material [39]. In this case, the properties that can be computed are not necessarily the desired effective properties but merely apparent properties of the investigated volume. By computing and averaging these properties for a sufficient number of realizations, the effective properties of heterogeneous materials can be estimated [39,58].

In such an approach, the representativity of the volumes depends on several parameters: the desired physical property and the targeted precision, the contrast between the properties of the constituents, the number of realizations and the volume fraction of the constituents. This statistical approach is suitable when the microstructure is simple enough to be generated by a random microstructural model. Combined with periodic boundary conditions, known to lead to the smallest boundary layer effects, smaller representative volume elements are therefore obtained. The microstructure of the fused-cast refractories is too complex to be described by such a microstructure model. The use of X-ray micro-computed tomography is therefore precious, but limits the size of the samples. Moreover, the use of periodic boundary conditions is not compatible with the mesh developed in this work.

Therefore, in this work, two different realizations of each material were considered. The representativity of these volumes for the creep properties at high temperature will

be discussed in Section 4.6. Covariance calculations, detailed in the next section, were performed to check that these volumes contain enough statistical information. Mixed boundary conditions were used for the computations. Creep tests were simulated by applying a pressure at the top face of the volumes. The displacement component along (Oz) of the bottom nodes was set to zero. Additional boundary conditions were introduced to fix the rigid body motions.

The notations used within the context of the mechanics of heterogeneous materials were as follows [59]: the local strain and stress fields inside the considered volume elements were denoted by $\varepsilon_{ij}(x_k)$ and $\sigma_{ij}(x_k)$. The macroscopic strain and stress tensors were then defined as the corresponding average values over each considered volume:

$$E_{ij} = \langle \varepsilon_{ij} \rangle = \frac{1}{V} \int_V \varepsilon_{ij}, dV, \quad \Sigma_{ij} = \langle \sigma_{ij} \rangle. \tag{7}$$

4. Results and discussion

The investigated volumes were composed of a stack of 2D slices along the z-axis. x and y represent the dimensions in µm of the 2D sections, whereas z is the thickness of the material. Due to the large size of the images, the dimensions of the investigated volumes were fixed to $(x = 336) \times (y = 310) \times (z = 1260)$ µm.

4.1. *Isotropy and selection of the as-received materials*

Figure 6 depicts, for each as-received material, the covariance function $C(h)$ of the zirconia phase according to the three directions (Ox), (Oy) and (Oz). For each material, the covariance is decreasing progressively as a function of the distance to reach an asymptote from a given distance, which is the range of the microstructure. For each material, the asymptote value is equal to the square of the volume fraction of the zirconia phase. Similar results were obtained according to the three directions, which suggests that the as-received materials are isotropic. The range of the microstructure, L_z, is 60 µm for the ZS12 material, 46 µm for the ZS18 material and 40 µm for the ZS24 material. It is worth mentioning that the zirconia entities
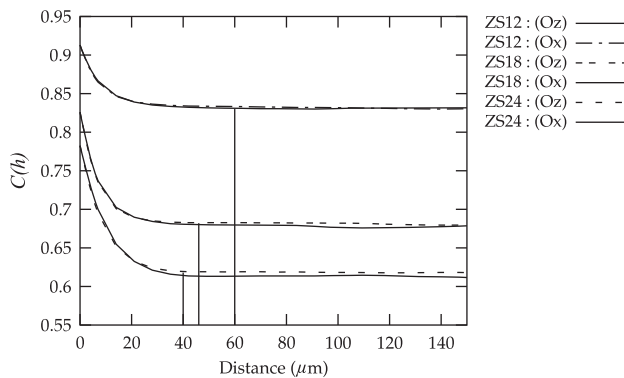

Figure 6. 3D covariance of the ZS12, ZS18 and ZS24 as-received materials according to the three directions (Ox), (Oy) and (Oz). For the sake of clarity, only (Oz) and (Ox) directions of one realization are represented. Volume dimensions are: $(x = 336) \times (y = 310) \times (z = 1260)$ µm.

that might look like isolated grains in Figure 1 are in fact sections of imbricated dendrites. When decreasing the amorphous phase content, the dendritic microstructure is so saturated that some interfaces between the dendrites may not be detected, even at high-magnification, leading to an overestimation of the zirconia skeleton continuity. L_z is characteristic of the size and spatial distribution of these zirconia entities, which are formed by heaps of dendrites, and is two to three times smaller than their average size, d ($d^{ZS12} = 200 \pm 73$ μm, $d^{ZS18} = 117 \pm 38$ μm, $d^{ZS24} = 79 \pm 22$ μm). We can therefore conclude that there is a dependence of the arrangement of the zirconia entities to a scale lower than half of their average size.

The zirconia grains are formed during a solidification process similar to metals [3]. It is well known in alloy solidification theory that the solute content has significant effects on grain refinement [60]. An increase in amorphous phase or solute content reduces the rate of crystal growth, which in turn increases the density of active particles for heterogeneous nucleation, reducing the size of the resulting dendrites and grains in the solidified microstructure [60]. The final grain size is the result of competition between heterogeneous
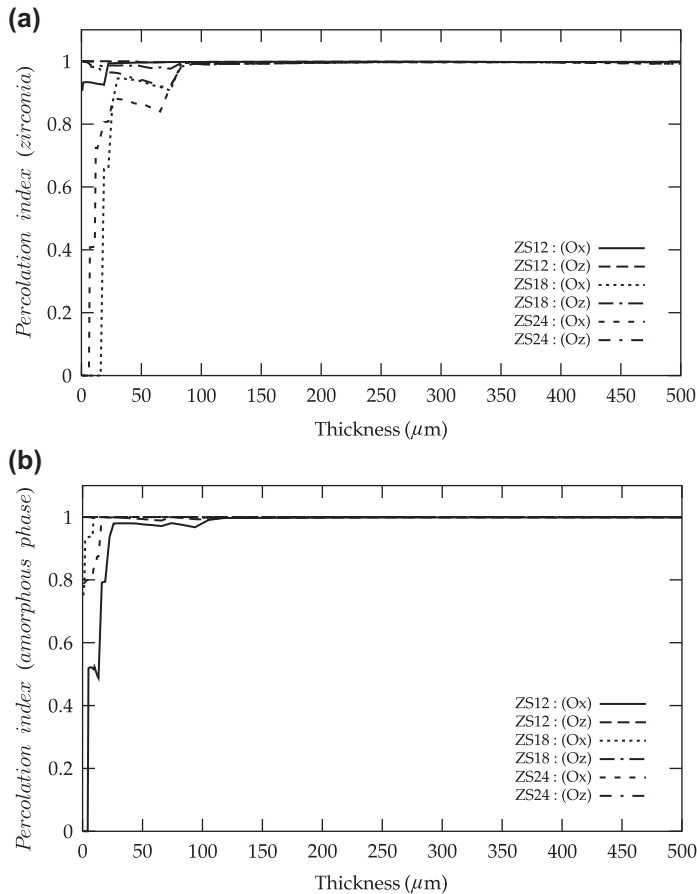

Figure 7. Evolution of the geometrical percolation index in (Ox) and (Oz) directions as a function of sample thickness: (a) zirconia, (b) amorphous phase. Similar results were obtained for the percolation index in the (Ox) and (Oy) directions and only (Ox) direction is represented. For the sake of clarity, the lower abscissa was reduced from 1200 to 500 μm. Volume dimensions are: $(x = 336) \times (y = 310) \times (z = 1260)$ μm.
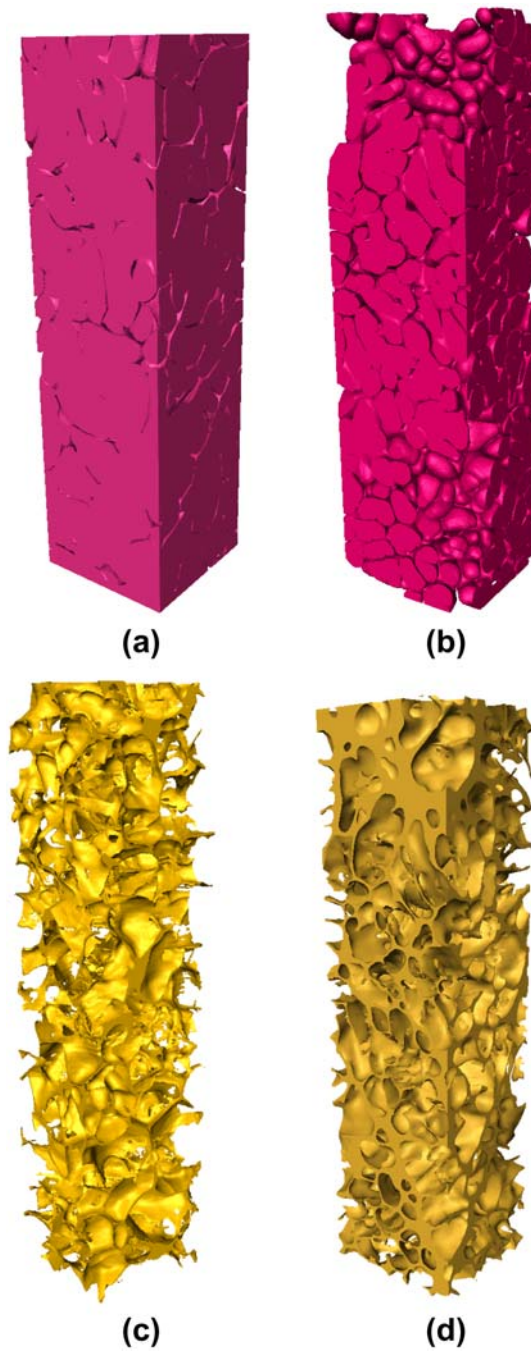
K. Madi et al.

Figure 8. (colour online) 3D representation of the interconnected parts of zirconia and amorphous phase: (a) zirconia (ZS12), (b) zirconia (ZS24), (c) amorphous phase (ZS12), (d) amorphous phase (ZS24). Volume dimensions are: $(x = 336) \times (y = 310) \times (z = 1260)\,\mu m$.
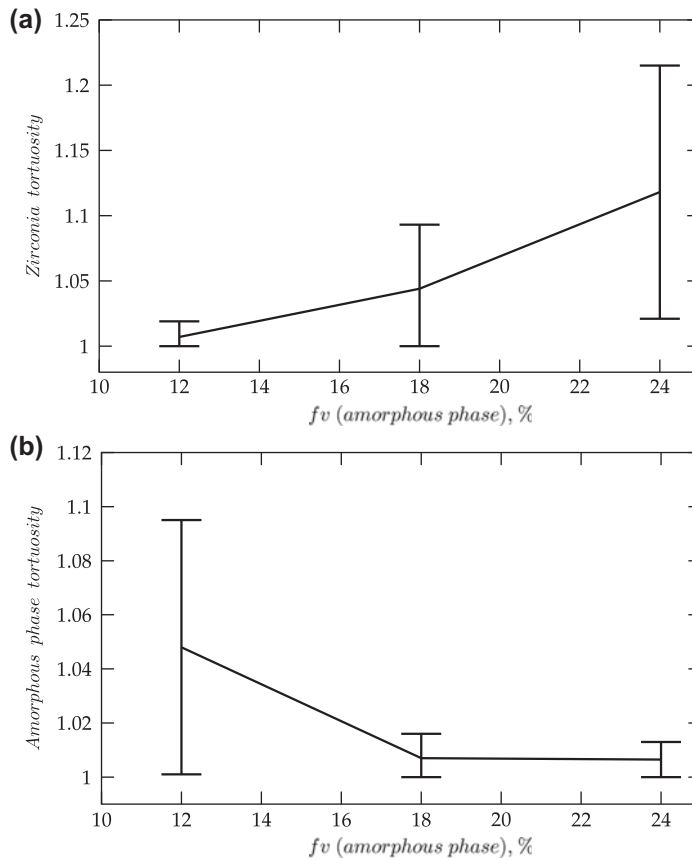
Figure 9. Tortuosity, according to (Oz) direction, vs. volume fraction of amorphous phase: (a) zirconia, (b) amorphous phase.

nucleation and growth. It is therefore logical that L_z decreases with increasing amorphous phase content.

The dimensions of the investigated volumes are very small compared to the dimensions of a refractory block. There is a huge factor of almost 10^9 between the volume of a refractory block and the investigated volumes. Therefore, the choice of the volumes must be carried out carefully to ensure representative statistical information. Two criteria were adopted: (i) the volume fraction of amorphous phase must be close to the average volume fraction of the considered material, (ii) the dimensions of the volume must be larger than the range of the microstructure. According to the covariance calculations performed on the as-received materials, the range of the microstructure, L_z, varies between 40 µm (ZS24 material) and 60 µm (ZS12 material), hence smaller than the dimensions of the investigated volumes.

4.2. *3D connectivity*

The evolution of the geometrical percolation index in (Ox), (Oy) and (Oz) directions was investigated for each phase as a function of the number of sections (*xy*) added in the thickness direction (Oz) (Figure 7). Similar results were obtained for the percolation index in the (Ox) and (Oy) directions. For the sake of clarity, only (Ox) direction is represented.
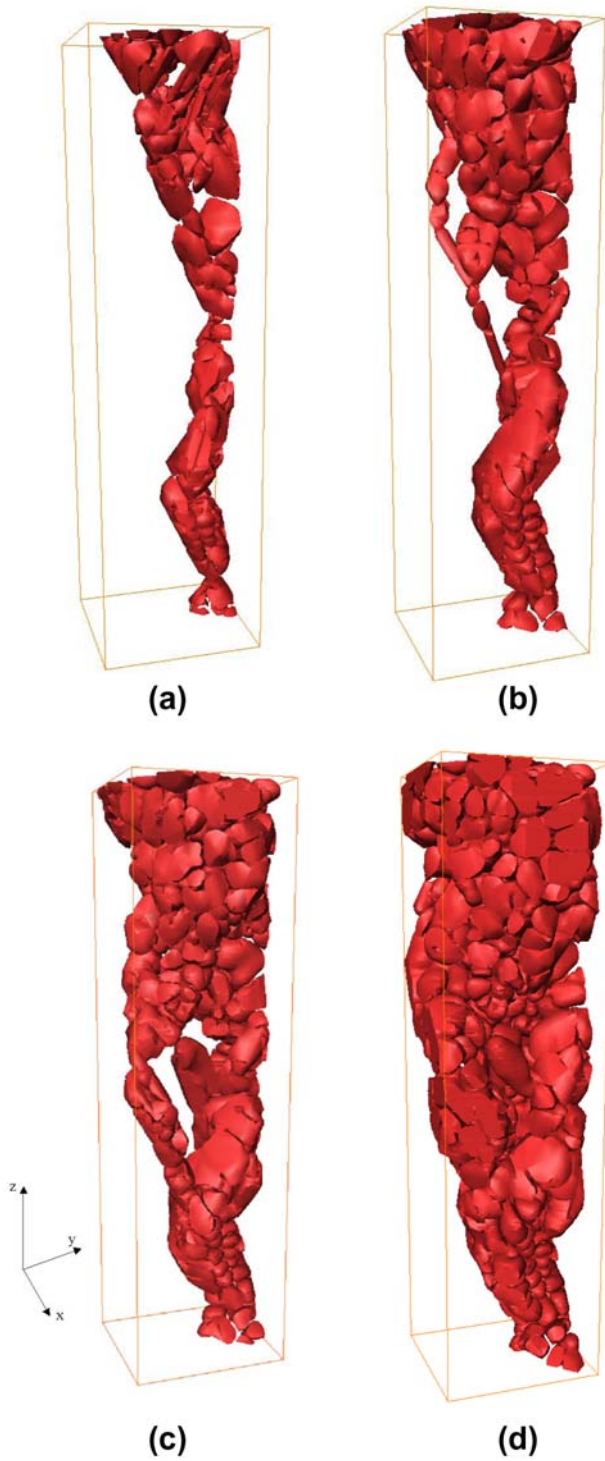
Figure 10. (colour online) 3D representation of the zirconia voxels of the ZS24 material having a tortuosity ranging between: (a) 1.005 et 1.02, (b) 1.01 et 1.03, (c) 1.01 et 1.07, (d) 1.01 et 1.12. Volume dimensions are: $(x = 336) \times (y = 310) \times (z = 1260)\,\mu\text{m}$.
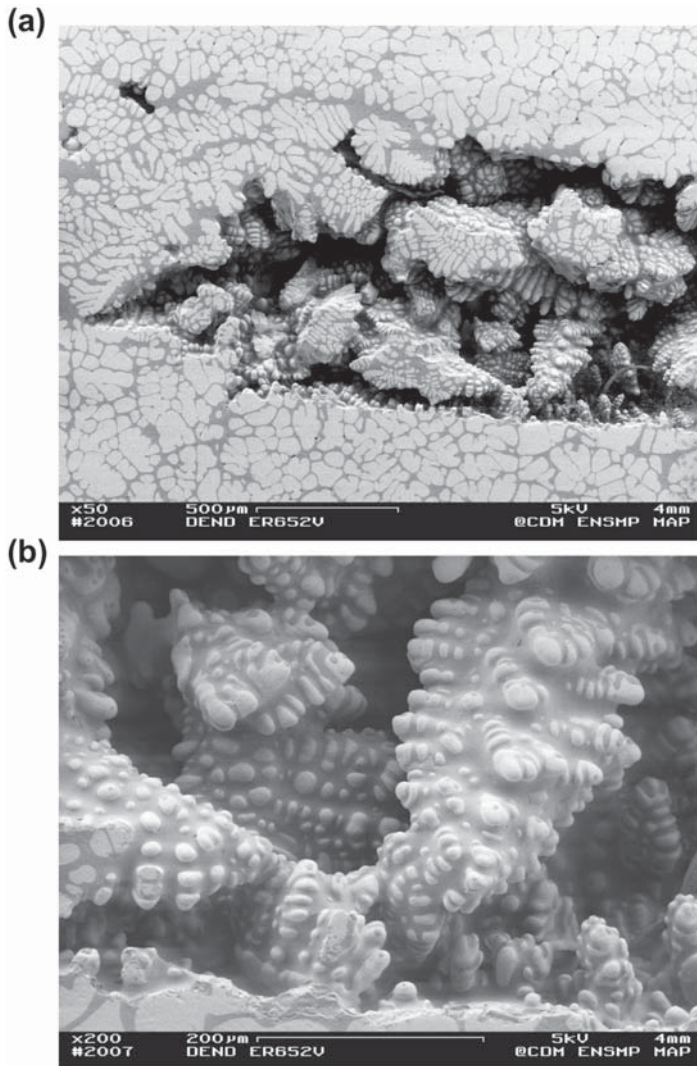
Figure 11. (a) SEM observation of the ZS24 material in a shrinkage cavity region, (b) dendrites surrounded by amorphous phase.

In the first section, for each material, the percolation index in (Oz) direction is very close to 1 for both phases. The percolation index in (Ox) direction rises with increasing thickness and also reaches the value of about 1 for a cumulated thickness of 40 μm for ZS12 and 166 μm for ZS18 and ZS24.

Such a percolation value means that the entire zirconia (resp. amorphous phase) is connected within the considered volumes. The small drops of the percolation index were attributed to the removal of isolated parts of zirconia phase (resp. amorphous phase) at the edges of the volumes. Figure 8 represents the set of all points in the zirconia phase (resp. amorphous phase) that can be linked together to the bottom and top faces of the volumes by paths entirely contained in the zirconia phase (resp. amorphous phase). When increasing the
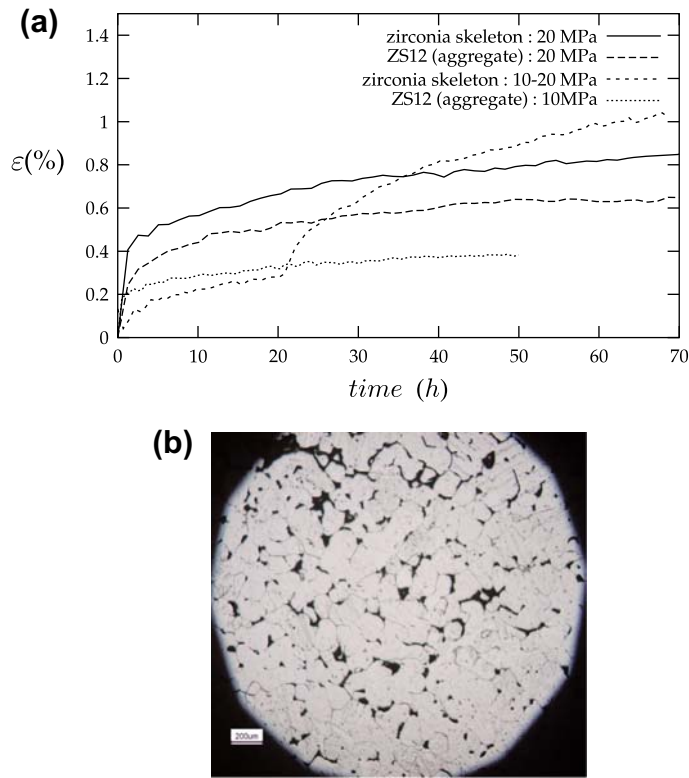
Figure 12. (colour online) (a) Creep curves of the ZS12 material and zirconia skeleton obtained at 1400°C, under stresses varying between 10 et 20 MPa, (b) Optical micrograph of the core of the zirconia skeleton after creep at 1400°C under 20 MPa. The black spots are pores that were created during the chemical attack and the polishing process due to the removal of isolated parts of zirconia.

volume fraction of amorphous phase, grain refinement is brought about by multiplication of dendrites (Figure 8(a) and (b)) resulting in thicker amorphous phase (Figure 8(c) and (d)). In the following section, the tortuosity of the zirconia phase will be studied in more detail and linked to the imbrication of the dendrites.

4.3. *Tortuosity*

For each phase of each material, the tortuosity has been calculated according to the (Oz) direction (largest dimension). Figure 9(a) and (b) depict for each phase the mean tortuosity and the corresponding standard deviation as a function of the volume fraction of amorphous phase. Doubling the amorphous phase content results in an increase of the mean tortuosity (resp. standard deviation) in the zirconia phase by about 10% (resp. 90%) and a decrease of the mean tortuosity (resp. standard deviation) in the amorphous phase by about 4% (resp. 86%). Due to the lack of tortuosity data in the literature for dendritic morphologies, our results cannot be compared. As a guide, in [40], the authors have calculated the tortuosity of a porous medium and linked it to the diffusion coefficient. They found tortuosities between 1 and 3.4.
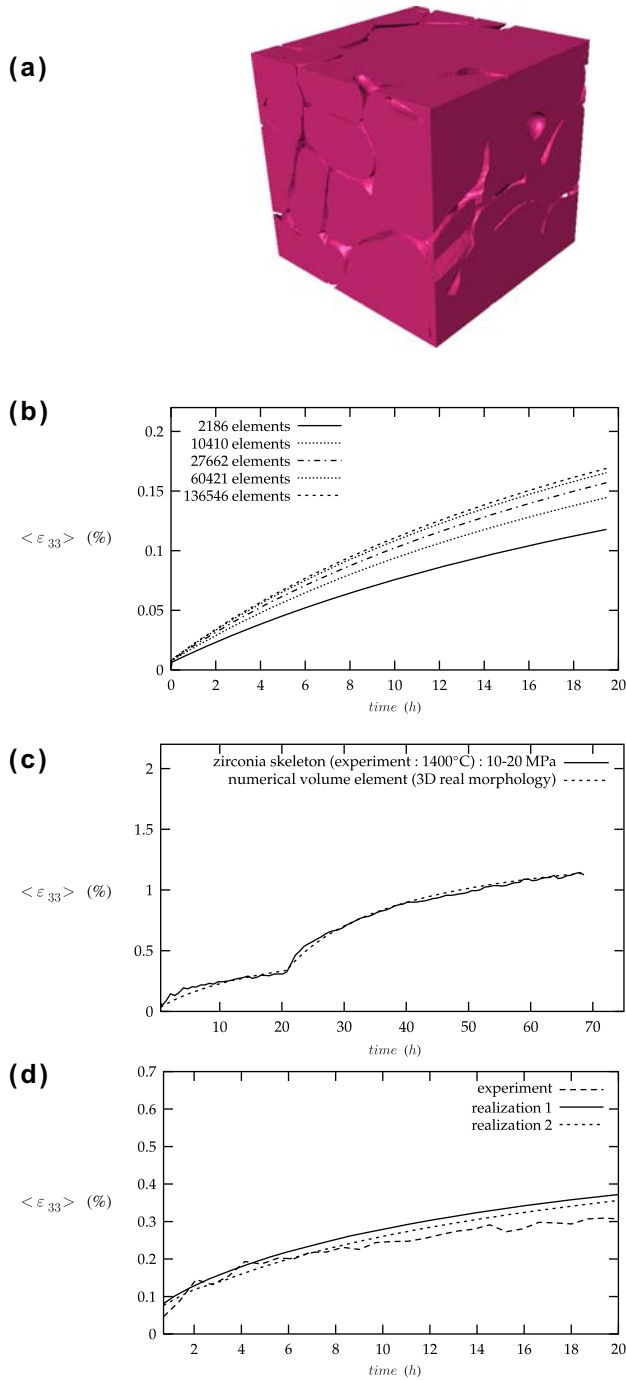
Figure 13. (colour online) (a) 3D representation of the cubic volume element (edge size: 200 μm) used to identify the creep law of the zirconia skeleton at 1400 °C, (b) effect of mesh density on the numerical creep response of the zirconia skeleton, (c) numerical and experimental creep curves of the zirconia skeleton at 1400 °C, under 10 and 20 MPa, (d) Numerical and experimental creep curves of the zirconia skeleton at 1400 °C, under 10 MPa (Volume dimensions are: 336 × 310 × 300 μm).

In the ZS12 material, at the end of the solidification process, the zirconia dendrites are so imbricated that some interfaces between the dendrites are difficult to detect, even when performing high-magnification observations by SEM. Therefore, the distance of the shortest paths connecting two opposite faces were very close to the euclidian distance (tortuosity close to 1). In the ZS24 material, however, longer paths were required in the zirconia phase due to grain refinement. The increase of amorphous phase thickness explains the decrease of the tortuosity in the amorphous phase.

Interestingly, thresholding the tortuosity of the zirconia phase contained in the ZS24 material at different intervals revealed the imbrication of the dendrites. This is confirmed in Figure 10 which represents 3D images of the zirconia voxels having a tortuosity ranging in the interval [1.005, 1.02], [1.01, 1.03], [1.01, 1.07] and [1.01, 1.12]. The classes are ranked in ascending order. When increasing the tortuosity class, the objects that appear seem to correspond to groups of dendrites. The latter are oriented differently and seem to perfectly interlock to form a zirconia skeleton. SEM observations of the ZS24 material in a shrinkage cavity region confirm the existence of dendrite groups (see Figure 11). Branches of dendrites, surrounded by the amorphous phase, with different orientations, can be seen in the core of the specimen and reflect the complexity of the microstructure. The zirconia phase is formed by a strong intrication of the dendrites (interlocking) which creates a continuous skeleton.

4.4. *Experimental characterization of the zirconia skeleton*

The procedure developed to eliminate the amorphous phase inside the ZS12 material was based on a chemical attack. The choice of the reactive was very important in order to limit the dissolution of the zirconia phase. The dissolution rate of the amorphous phase in the reactive must be much faster than that of the zirconia. In our case, fluorhydric acid (HF) was chosen as reactive, because it is known to have a corrosive effect on silica and silicates and, according to [61], the dissolution rate of zirconia in HF is low. When dipping the samples in the HF solution, a reaction front is propagating from the free surface to the core of the material. Three parameters were then optimised after several tests: the size of the samples, the concentration of the HF solution and the attack duration. The position of the front was observed on the surface and in the core of the material using optical microscopy. In our case, cylinders of 3 mm diameter and 11 mm height were chosen and the best attack conditions were in a 8% HF solution during 24 h. The porous zirconia skeleton obtained after removing the amorphous phase had a poor bending strength but a good compressive resistance. To verify this asumption, several compressive creep tests were performed on the zirconia skeleton of the ZS12 material, at 1400 °C, under stresses varying between 10 and 20 MPa. Results are illustrated in Figure 12(a) where a comparison is made with the ZS12 material. Creep curves are very similar and optical microscopy observations, performed before and after the tests, confirmed that no significant damage developed in the zirconia skeleton (see Figure 12(b)).

A complementary investigation to reveal a possible damage of the zirconia skeleton after elimination of the amorphous phase was undertaken recently by Ding [62]. In addition to microstructural observations (SEM), two kinds of tests were performed: (i) Vickers hardness tests in the same zirconia region before and after attack, and (ii) monotonic compressive tests at high temperature (1100 °C) on as-received and attacked samples. In both cases, similar results were obtained before and after removal of the amorphous phase, confirming that the zirconia skeleton was not significantly affected by the chemical attack.

This section validates the fact that the zirconia skeleton is mainly responsible for the high creep resistance observed at high temperature. The following step consists in identifying a creep law for the zirconia skeleton.

4.5. *Identification of the zirconia skeleton creep law at* 1400 °C

Compressive creep tests were performed on zirconia skeletons under stresses varying between 10 and 20 MPa. A power creep law with kinematic hardening, described in Section 3.2, was then identified from these results. An inverse method based on a finite-element model that takes into account the 3D real morphology of the zirconia skeleton was used. The four parameters of the model n, K, C and D were extracted using an optimization method based on the Levenberg–Marquardt algorithm and implemented in the finite-element code Zset [57].

To reduce the computation time, a cube of edge length 200 μm was used for the identification (see Figure 13(a)) and was selected so that the volume fraction of the zirconia phase was close to the nominal value (87.2 vs. 88%). Prior to the optimization, a sensitivity analysis was performed to select the number of elements. The analysis was conducted with an initial guess of parameters, so that the creep response was close to the experiment. The results, illustrated in Figure 13(b), show the convergence of the macroscopic strain as a function of the number of elements, during a creep test at 10 MPa where a pressure was applied at the top face of the cube ($z = 200$ μm). A mesh density of about 300 μm^3/element (27662 quadratic elements) is necessary to get an accuracy of 5% on the mean strain. The optimization was then carried out using this mesh density. A first creep test was performed at 10 MPa, followed by a second creep test performed at 20 MPa. At each step of the optimization procedure, the numerical average deformation $\langle \varepsilon_{33} \rangle$ was thus compared to the experimental deformation. The values of the fitted parameters are reported in Table 2. Figure 13(c) depicts the numerical creep response of the simulated volume from this set of parameters. This curve describes the experimental result correctly. A few comments can be made on the obtained creep law. In simple tensile-compressive loadings, the internal back stress is changing with time and converges towards the ratio $\frac{C}{D}$. In our case, this limit value is close to 117 MPa at 1400 °C. Thus, the fitted creep law only describes primary creep. The experiment is not long enough to highlight an obvious steady-state creep.

4.6. *Simulation of the creep behaviour of the two-phase material at* 1400 °C

This section aims at simulating the compressive creep behaviour of the materials at 1400 °C. At this temperature, the percolating amorphous phase behaves like a Newtonian fluid and played a negligible role on the mechanical resistance. The aggregate deformation was controlled by the rheology of the ziconia phase. To verify this assumption, the numerical creep responses of the ZS12 material with and without the amorphous phase have been compared. The creep responses of the ZS12, ZS18 and ZS24 materials were then simulated on larger volumes, using the zirconia creep law identified in Section 4.5. Finally, the effect of microstructure variability and the evolution of the local stresses in the zirconia phase were investigated during the creep experiment. All the calculations were performed with a fixed mesh density of 300 μm^3/element (10-node quadratic tetrahedra) and boundary conditions similar to those described in Section 4.5.

4.6.1. *Contribution of the amorphous phase to the overall response*

To demonstrate that the effect of the amorphous phase on the aggregate deformation is negligible, a small volume can be used. The chosen volume is the one used for the optimization procedure in Section 4.5. Two creep tests were simulated with and without the amorphous phase, at 1400 °C under 10 and 20 MPa. The macroscopic stress Σ_{33} was applied according to the (Oz) direction. As expected, the obtained average deformations $\langle\varepsilon_{33}\rangle$ are similar, as illustrated in Figure 14(a), as well as the local stresses in the zirconia phase (see Figure 14(b) and (c)). In the following sections, the amorphous phase will not be considered.
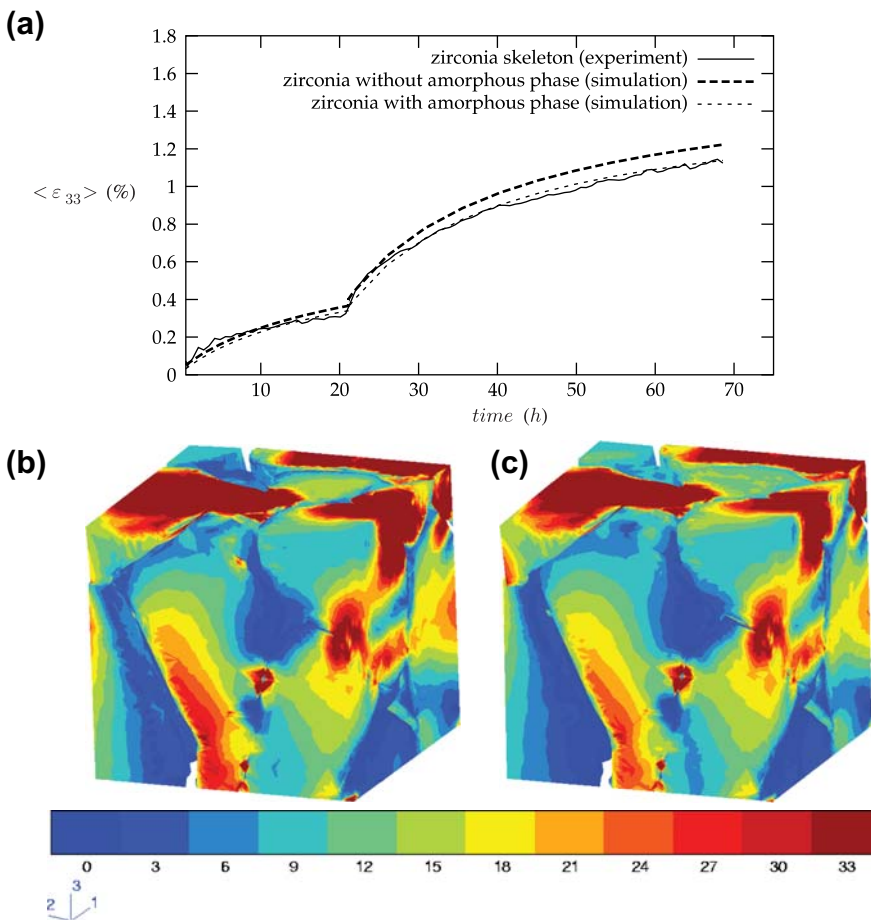

Figure 14. (colour online) (a) Creep simulation of the ZS12 material, at 1400 °C under 10 and 20 MPa, obtained with and without the amorphous phase (cube of size 200 μm^3). Contour of von Mises equivalent stress (in MPa) in the zirconia skeleton after 6 hours creeping at 1400 °C under 10 MPa: (b) simulation with amorphous phase, (c) simulation without amorphous phase.

4.6.2. *Simulation of the creep behaviour of the ZS12 material and effect of microstructure variability*

The creep law was tested on larger zirconia volumes illustrated in Figure 4(b) and (c). The volume fractions of zirconia were 88.4 and 87.7%. Creep tests were simulated at 1400 °C, under a macroscopic stress Σ_{33} of 10 MPa according to the (Oz) direction. The numerical average deformation $\langle \varepsilon_{33} \rangle$ of the ZS12 material, depicted in Figure 13(d), is similar from one realization to another and in good agreement with the experiments. This validates the representativity of the considered volumes.

It is observed in Figure 12(a) that the experimental creep curve without amorphous phase (zirconia skeleton) may be even higher than the one with the amorphous phase (ZS12). Fused-cast refractories have very heterogeneous microstructures and microstructure variability is likely to explain this result. To test this hypothesis, creep tests were simulated at 1400 °C under 20 MPa on three zirconia volumes randomly extracted from two cylinders (cylinder 1: realization 1 (89% of zirconia), realization 2 (92.5% of zirconia); cylinder 2: realization 1 (90% of zirconia). The results are represented in Figure 15. The volumes with volume fractions of 90 and 89% exhibit a creep response similar to the experimental curve of the zirconia skeleton. The creep curve of the volume having a volume fraction of 92.5% is lower than the experimental creep curves (zirconia skeleton and ZS12). This suggests that the zirconia volume fraction of the experimentally tested sample without amorphous phase (zirconia skeleton) was close to the nominal value (88%), while that of the experimentally tested sample with amorphous phase (ZS12) probably ranged between 90 and 92.5%.

4.6.3. *Creep responses of the materials with higher contents of amorphous phase*

Creep tests were simulated on the ZS18 and ZS24 materials, at 1400 °C under 12 MPa, using the same zirconia creep law identified on the ZS12 material. The volumes are represented in Figure 5 and the results depicted in Figure 16. Although the experiment is not long enough to highlight an obvious steady-state regime, the models provide a realistic description of the creep rate and strains. However, the models are not able to properly capture the
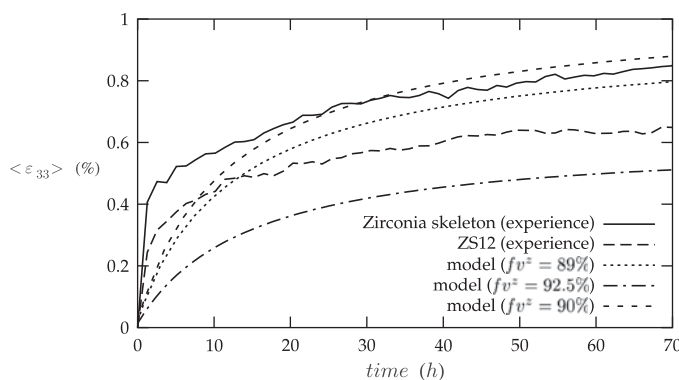

Figure 15. Effect of microstructure variability on the numerical creep reponse of the ZS12 material, at 1400 °C under 20 MPa. fv^z represents the volume fraction of zirconia. Volume dimensions are: $336 \times 310 \times 300$ μm.
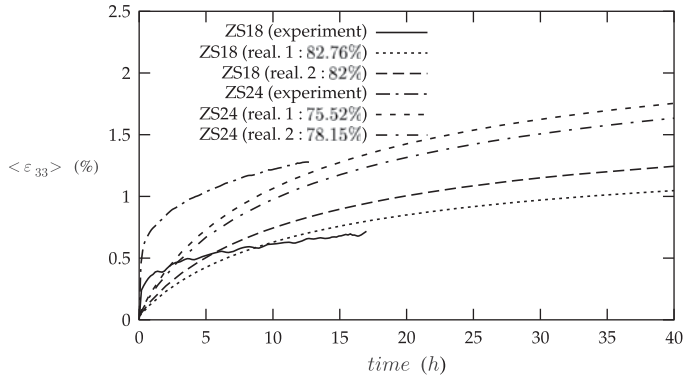
Figure 16. Creep simulation of the ZS18 and ZS24 materials, at 1400°C under 12 MPa, using the zirconia creep law identified in Section 4.5. Volume dimensions are: $336 \times 310 \times 300\,\mu m$.

primary creep, which might be attributed to the size of the microstructural models and/or microstructure variability of the tested samples.

4.6.4. *Evolution of the stresses in the zirconia phase*

In this section, the local stresses in the zirconia phase of ZS12, ZS18 and ZS24 materials are investigated during a creep test at 1400 °C under 10 MPa. The volumes are represented in Figures 4 and 5 (dimensions: $336 \times 310 \times 300\,\mu m$). The histograms for von Mises stress component σ_{mises} in zirconia are given for each material in Figure 17(a). Such histograms were obtained by storing the σ_{mises} component at all integration points inside the zirconia phase elements after 20 hours of creep. The meshing of the microstructure contained 120000 integration points. These values were then ranked to construct the stress distribution function. The frequency represents the volume fraction of the zirconia phase where the local von Mises stress takes the value $\sigma_{mises} \pm \Delta\sigma_{mises}$ on the horizontal axis and where $\Delta\sigma_{mises} = 1$ MPa is the class interval size. Compared to the ZS12 material, the distributions of the ZS18 and ZS24 materials are more scattered. These histograms are completed by contour of the von Mises stress in a section extracted at the core of the material (see Figure 17(b) and (c)). It is shown that the highest stresses are reached in the regions where the zirconia is strongly interconnected. In some points, the stress levels reach more than three times the value of the macroscopically applied stress.

5. Summary and conclusions

This work aimed at investigating the link between the amorphous phase content, the zirconia skeleton morphology and the material creep behaviour at high temperature. The zirconia phase, the main part of the refractory (88% vol.), is essentially constituted of an interlocked continuous skeleton created by the dendritic growth of the zirconia crystals within the liquid phase. When increasing the volume fraction of amorphous phase, the zirconia phase remains continuously connected but grain refinement is brought about by multiplication of dendrites, resulting in a thicker amorphous phase and a more tortuous zirconia network. Outstanding creep resistance was observed, even for large amount of amorphous phase,
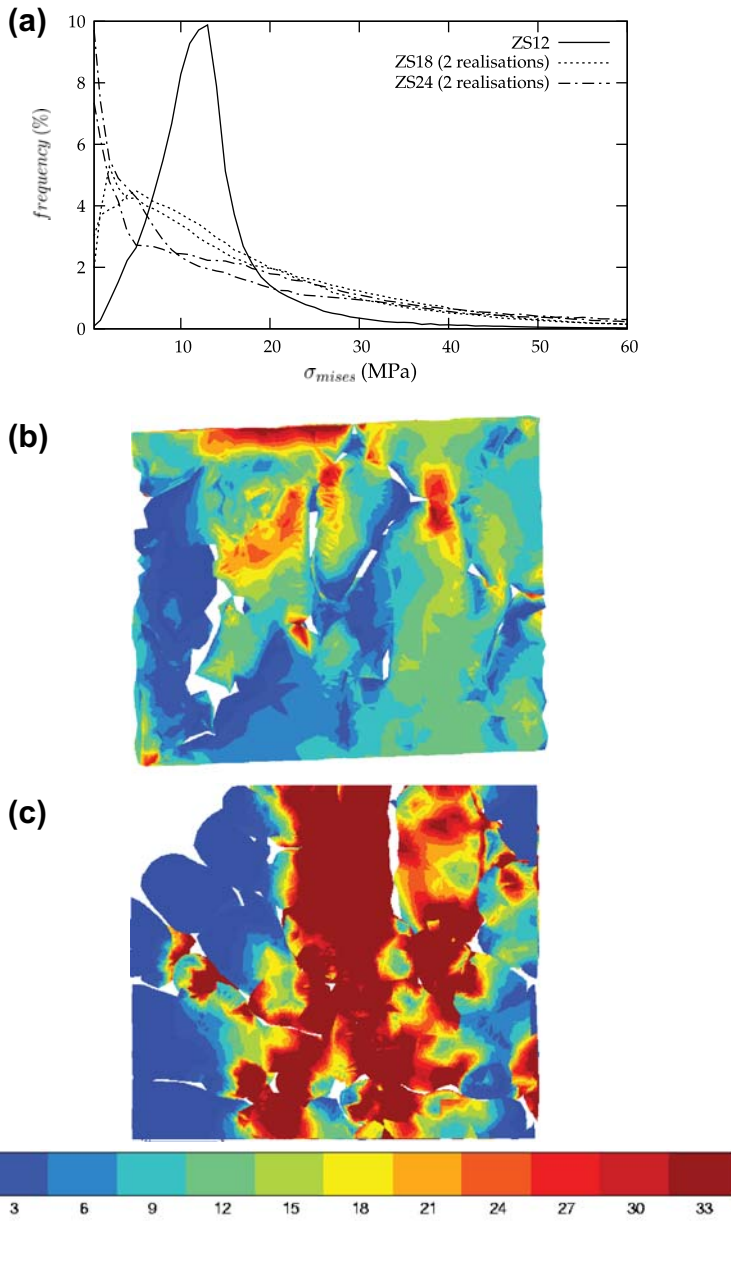
Figure 17. (colour online) Simulation of the creep behaviour of the zirconia skeleton: (a) distribution of the local von Mises stress, σ_{mises} (MPa), vs. volume fraction of amorphous phase at 1400 °C, under 10 MPa. Contour of the von Mises stress, σ_{mises} (MPa), in a section extracted at the core of the zirconia skeleton (section yz), after 20 h of creep, under 10 MPa: (b) ZS12, (c) ZS24. The macroscopic stress Σ_{33} was applied according to (Oz) direction. Section dimensions are: $310 \times 300\,\mu$m.

at temperatures about twice the glass transition temperature of the amorphous phase. This fundamentally contrasts with sintered, granular materials, where grain boundary sliding and grain interlocking are often the predominant deformation mechanisms at high temperature [63,64]. In sintered ceramics, for such amount of amorphous phase (12 to 24% vol.), the creep rate increases drastically with increased temperature [63,64].

The high connectivity of the zirconia explains the high creep strength and corrosion resistance of fused-cast refractories when compared to most of sintered materials [29]. Although the amorphous phase has no structural role at high temperature, it has a direct impact on the geometry of the zirconia skeleton during solidification, which in turn controls the deformation. This is an important finding which opens the way to further experimental protocols in the near future to guide the design of new products.

A 3D finite-element model based on the 3D real morphology of the microstructure was developed to describe the creep behaviour of the ZS12 material at 1400 °C as measured. The zirconia creep law was identified by an inverse method at 1400 °C, from its 3D real morphology. A good agreement was found for the ZS12 material between numerical and experimental creep tests. Using the zirconia creep law identified for the ZS12 material, the models were used to predict the creep responses of the materials with higher contents of amorphous phase (ZS18/ZS24 materials). The models provided a realistic description of the creep rate and strains. Further computations on larger volumes and more experimental tests will be required to investigate the capacity of the models to correctly describe the primary creep. The rheology of the aggregate at high temperature is mainly controlled by the zirconia phase. The exploitation of complementary techniques at lower scales and the development of *in situ* creep measurements should provide us more data in the future to better understand the deformation mechanisms that are activated in the zirconia at high temperature.

Acknowledgements

References

[1] M. Boussuge, *Study of thermomechanical properties of industrial refractories: The french program Prometheref*, in *UNITECR 2003 Proceedings, 8th biennal worldwide conf. on refractories*, Osaka international convention center, Osaka, October 19–22, 2003, p.513.

[2] M. Boussuge, Key Eng. Mater. 264–268 (2004) p.1755.

[3] M. Boussuge, J. Mater. Sci. 43 (2008) p.4069.

[4] L. Massard, *Study of the creep behavior of fused-cast refractories belonging to the Alumina-Zirconia-Silica system (in French)* [PhD Thesis]. Ecole Nationale Supérieure des Mines de Paris, 2005.

[5] E. Yeugo-Fogaing, *High temperature properties of fused-cast refractories and refractory concretes (in French)* [PhD Thesis]. ENSCI Limoges, 2006.

[6] E. Yeugo-Fogaing, Y. Lorgouilloux, M. Huger and C. Gault, J. Mater. Sci. 41 (2006) p.7663.

[7] E. Yeugo-Fogaing, M. Huger and C. Gault, J. Eur. Ceram. Soc. 27 (2007) p.1843.

[8] E. Lataste, *Thermomechanical behavior and damage of zirconia fused-cast refractories (in French)* [PhD Thesis]. Institut National des Sciences Appliquées de Lyon, 2005.

[9] E. Lataste, J.P. Erauw, C. Olagnon, G. Fantozzi and J. Eur, J. Eur. Ceram. Soc. 29 (2009) p.587.

[10] K. Madi, *Influence of three-dimensional morphology on the mechanical behavior of fused-cast refractories (in French)* [PhD Thesis]. Mines-ParisTech, 2006.

[11] K. Madi, S. Forest, M. Boussuge, S. Gailliègue, E. Lataste, J.Y. Buffière, D. Jeulin and D. Bernard, Comput. Mater. Sci. 39 (2007) p.224.

[12] A. Molinari, G.R. Canova and S. Ahzi, Acta Metall. 35 (1987) p.2983.

[13] A. Zaoui and R. Masson, *Modelling stress dependent transformation strains of heterogeneous materials*, in *Transformation problems in composite and active materials*, Y.A. Bahei-El-Din and G.J. Dvorak, eds., Kluwer Academic Publishers, Dordrecht, 1998, p.3.

[14] G. Canova, H. Wenk and A. Molinari, Acta Metall. et Mater. 40 (1992) p.1519.

[15] R. McLaughlin, Int. J. Eng. Sci. 15 (1977) p.237.

[16] S. Hollister, J. Brennan and N. Kikuchi, J. Biomech. 27 (1994) p.433.

[17] B. Van Rietbergen, H. Weinans, R. Huiskes and B. Polman, Inter. J. Numer. Meth. Eng. 39 (1996) p.2743.

[18] R. Muller and P. Ruegsegger, Med. Eng. Phys. 17 (1995) p.126.

[19] S. Youssef, E. Maire and R. Gaertner, Acta Mater. 53 (2005) p.719.

[20] S. McDonald, G. Dedreuil-Monet, A. Alderson, Y.T. Yao and P. Withers, Phys. Status Solidi. B 248 (2011) p.45.

[21] N. Lippmann, T. Steinkopf, S. Schmauder and P. Gumbsch, Comp. Mater. Sci. 9 (1997) p.28.

[22] F. Barbe, L. Decker, D. Jeulin and G. Cailletaud, Int. J. Plast. 17 (2001) p.513.

[23] F. Barbe, S. Forest and G. Cailletaud, Int. J. Plast. 17 (2001) p.537.

[24] M. Nygards and P. Gudmundson, Comput. Mater. Sci. 24 (2002) p.513.

[25] C. Hartig and H. Mecking, Comput. Mater. Sci. 32 (2005) p.370.

[26] J. Wismans, J. van Dommelen, L. Govaert and H. Meijer, Mater. Sci. Forum 638–642 (2010) p.2761.

[27] K.A. Jackson and J.D. Hunt, Acta Met. 13 (1965) p.1212.

[28] K.A. Jackson, *Crystal growth kinetics and morphology*, in *Proceedings of an International Symposium on Special Topics in Ceramics: Kinetics of reactions in ionic systems*, T.J. Gray and V.D. Frèchette, eds., Plenum Press, New York, 1967, p. 229.

[29] A.M. Alper, *Microstructures developed from fusion casting*, in *Proceedings of the Third Int. Materials, symposium "Ceramic microstructures, their analysis, significance and production"*, R.M. Fulrath andJ.A. Pask, eds., John Wiley and Sons, New York, London, Sydney, 1966, p.763.

[30] A.M. Alper, R.C. Doman, R.N. Mc Nally and H.C. Yeh, *The use of phase diagrams in fusion-cast refractory materials research*, in *Phase Diagrams*, A.M. Alper, ed., Academic Press, London, 1970, p.117.

[31] M. Gaubil, *Solidification studies of refractory ceramics belonging to the quaternary system Al2O3-ZrO2-SiO2-Na2O (in French)* [PhD Thesis]. Universitè d'Orlèans, 1996.

[32] G. Matheron, *The regionalized variables and their estimation: An application of the theory of random functions to natural sciences*, Masson, Paris, 1965.

[33] J. Serra, Image Analysis and Mathematical Morphology, Academic Press, London, 1982.

[34] E. Maire, J.Y. Buffière, L. Salvo, J. Blandin, W. Ludwig and J. Letang, Adv. Eng. Mater. 3 (2001) p.539.

[35] D. Bernard, Oil Gas Sci. Technol-Rev. IFP 60 (2005) p.747.

[36] D. Bernard, A. Chirazi. *Numerically enhanced microtomographic imaging method using a novel ring artefact filter*, in *Advances in X-ray tomography for geomaterials*, J. Desrues, G. Viggiani and P. Bèsuelle, eds., ISTE, London, 2006, p.117.

[37] D. Jeulin, *Mathematical morphology and multiphase materials*, in *Proceedings of 3rd European Symposium for Stereology*, M. Kalisnik ed., Committee for Culture and Science & Društvo anatoma Jugoslavije, Stereological Section, Ljubljana, 1981, p.265.

[38] D. Jeulin, *Morphological characterization and models of random sets*, in *Homogénéisation en mécanique des matériaux, Tome 1: Matériaux alèatoires élastiques et milieux périodiques*, M. Bornert, T. Bretheau and P. Gilormini, eds., Hermés Science Publications, Paris, 2001, p.95.

[39] T. Kanit, S. Forest, I. Galliet, V. Mounoury and D. Jeulin, Int. J. Solids Struct. 40 (2003) p.3647.

[40] L. Decker, D. Jeulin and I. Tovena, Acta Stereol. 17 (1998) p.107.

[41] R. Lerallut, *Image modeling and understanding using graph (in French)* [PhD Thesis]. Mines-ParisTech, 2006.

[42] M. Boussuge, *Contribution to studies of high temperature mechanical behavior of silicium nitride and carbide: critical use of double-torsion test (in French)* [PhD Thesis]. Ecole Nationale Supèrieure desMines de Paris, 1985.

[43] P. Vivier, *Strengthening and slow crack growth in silicon carbide and silicon nitride: local approach of the viscoplastic behaviour (in French)* [PhD Thesis]. Ecole Nationale Supèrieure des Mines de Paris, 1988.

[44] W. Lorensen and H. Cline, Comput. Graphics 21 (1987) p.163.

[45] Avizo, (1997), An advanced 3d visualisation and volume modeling system. http://www.amira.com, http://wwww.vsg3d.com

[46] P.J. Frey, H. Borouchaki and P.L. George, Comput. Methods Appl. Mech. Eng. 157 (1998) p.115.

[47] D. Gomez-Garcia, J. Martinez-Fernandez, A. Dominguez-Rodriguez, P. Eveno and J. Castaing, Acta Mater. 44 (1996) p.991.

[48] J. Chevalier, C. Olagnon, G. Fantozzi and H. Gros, J. Eur. Ceram. Soc. 17 (1997) p.859.

[49] D.M. Owen and A.H. Chokshi, Acta Mater. 46 (1998) p.667.

[50] A.H. Chokshi, Scr. Mater. 42 (2000) p.241.

[51] A.H. Chokshi, Scr. Mater. 48 (2003) p.791.

[52] R. Schaller, M. Daraktchiev and S. Testu, Mater. Sci. Eng. A 387–389 (2004) p.687.

[53] J.M. Calderon-Moreno, A.R. de Arellano-Lopez, A. Dominguez-Rodriguez and J.L. Routbort, J. Eur. Ceram. Soc. 15 (1995) p.983.

[54] C. Lorenzo-Martin, D. Gomez-Garcia, A. Gallardo-Lopez, A. Dominguez-Rodriguez and R. Chaim, Scr. Mater. 50 (2004) p.1151.

[55] B. Amana, R. Duclos and J. Crampon, Ceram. Int. 18 (1992) p.385.

[56] J. Lemaitre and J.L. Chaboche, *Mécanique des matériaux solides*, 2nd ed., Dunod, Paris, 1996,

[57] ZseT/ZéBuloN, User manual. emp/lmr/nwnm/onera, 1997.

[58] K. Madi, S. Forest, M. Boussuge and D. Jeulin, *Estimating RVE sizes for 2D/3D viscoplastic composite materials*, in *Matériaux 2006 Proceedings*, edited by SF2M, 2006.

[59] P. Suquet, *Continuum micromechanics, CISM Courses and Lectures No. 377*, Springer Verlag, 1997.

[60] H. Men and Z. Fan, Acta Mat. 59 (2011) p.2704.

[61] F. Shojai and T.A. Mantyla, Ceram. Int. 27 (2001) p.299.

[62] Y. Ding, *Relations between the three-dimensional microstructure and the mechanical properties of zirconia fused-cast refractories (in French)* [PhD Thesis]. Mines-ParisTech, 2012.

[63] H. Muto and M. Sakai, J. Am. Ceram. Soc. 81 (1998) p.1611.

[64] D. Wilkinson, J. Am. Ceram. Soc. 81 (1998) p.275.